Official Journal of CIOMP
elight.springeropen.com

RESEARCH ARTICLE

Open Access

Revealing the output power potential of bifacial monolithic all-perovskite tandem solar cells

Hongjiang Li†, Yurui Wang†, Han Gao†, Mei Zhang, Renxing Lin, Pu Wu, Ke Xiao and Hairen Tan*

Abstract

Bifacial monolithic all-perovskite tandem solar cells have the promise of delivering higher output power density by inheriting the advantages of both tandem and bifacial architectures simultaneously. Herein, we demonstrate, for the first time, the bifacial monolithic all-perovskite tandem solar cells and reveal their output power potential. The bifacial tandems are realized by replacing the rear metal electrodes of monofacial tandems with transparent conduction oxide electrodes. Bandgap engineering is deployed to achieve current matching under various rear illumination conditions. The bifacial tandems show a high output power density of 28.51 mW cm^{-2} under a realistic rear illumination (30 mW cm^{-2}). Further energy yield calculation shows substantial energy yield gain for bifacial tandems compared with the monofacial tandems under various ground albedo for different climatic conditions. This work provides a new device architecture for higher output power for all-perovskite tandem solar cells under real-world conditions.

Keywords: Bifacial tandems, All-perovskite tandem solar cells, Bandgap engineering, Energy yield, Stability

1 Introduction

Metal halide perovskite solar cells have attracted enormous attention as their power conversion efficiencies (PCEs) rapidly increase from below 4% to over 25% [1, 2]. Further improving the performance with low additional costs is crucial for the commercialization of perovskite solar cells. One of the most promising routes is to adopt the tandem configuration to overcome the Shockley-Queisser limit of single-junction solar cells [3, 4]. By stacking two absorbers with complementary bandgap, tandem solar cells promise higher PCEs than their single-junction counterparts by reducing thermalization loss and increasing spectral utilization range. Due to their widely tunable bandgap from 1.2 to 2.3 eV via composition engineering [5, 6], long carrier diffusion length [7], high absorption [8], and low non-radiative recombination rate [9], perovskites are highly desirable for tandem solar cells, including perovskite/Si [10–12], perovskite/CIGS [13, 14], perovskite/organic, [15, 16] and perovskite/perovskite tandem solar cells [17, 18]. Among them, all-perovskite (perovskite/perovskite) tandem solar cells are highly promising due to their low cost, high specific power, and flexibility [19–21].

After the first demonstration of the monolithic all-perovskite tandem solar cells with a PCE of 17.0% [18], the PCE of monolithic all-perovskite tandems have been fastly improved to the recently certified value of 28.0% [17, 24], exceeding the single junction perovskite solar cells with a certified PCE of 25.7% [25]. Despite those encouraging advancements, other strategies for achieving higher output power density (OPD) are still highly desired to bring down the levelized cost of energy (LCOE), which is the key to their commercialization. Besides using tandem architecture, another effective strategy to increase the OPD of perovskite solar cells is to take the advantage of bifacial configuration [26, 27],

†Hongjiang Li, Yurui Wang, and Han Gao contributed equally to this work

*Correspondence: hairentan@nju.edu.cn

Jiangsu Key Laboratory of Artificial Functional Materials, College of Engineering and Applied Sciences, National Laboratory of Solid State Microstructures, Nanjing University, Nanjing 210023, China

which allows significant OPD gain by utilizing the light reaching the back side of the devices, namely the albedo (the reflected and scattered light from the surroundings). By using transparent conductive oxide (TCO) as rear electrodes, bifacial perovskite solar cells can be constructed based on the well-established monofacial configuration [28]. More importantly, bifacial perovskite solar cells would be more stable than their monoficial counterparts since the TCO based rear electrodes are tolerant to halide corrosion and act as a diffusion-blocking barrier [29]. Numerical simulation shows that bifacial tandem cells can inherit the advantages of tandem architecture and bifacial design, allowing higher thermodynamic efficiency beyond monofacial tandems and single-junction bifacial solar cells [30–32]. Recently, bifacial perovkite/silicon tandem solar cells with an OPD of ~ 26 mW cm^{-2} (monofacial efficiency of 25.2%) was demonstrated via bandgap engineering [33]. However, in the presence of albedo, the optimized current matching design in monofacial tandems will lead to current mismatch in bifacial configuration, since only the current of the bottom subcells will be increased with albedo in bifacial monolithic tandems [33, 34]. In addition, the rear transparent electrodes will reduce the current in the bottom subcells by allowing light to transmit without rear reflection compared to monofacial tandems [32]. Therefore, the current matching is required to be redesigned in bifacial tandem configurations.

Herein, for the first time we experimentally demonstrate the design and fabrication of bifacial all-perovskite tandem solar cells by using TCO as the rear electrode. Bandgap engineering of the top subcell was deployed to obtain current matching under various rear illumination. The effect of albedo on the photovoltaic parameters and spectral response have been systematically investigated. Energy yield calculation reveals higher output power density by utilizing bifacial architechture under real-world conditions.

2 Results

Figure 1a, b shows the schematic stack and cross-sectional scanning electron microscopy (SEM) image of bifacial all-perovskite tandem solar cell consisting of wide-bandgap and narrow-bandgap perovskite subcells, and a tunnel junction for electrical connection of the two subcells. To harvest light reflected by the ground and surrounding, and diffuse skylight, the opaque rear metal electrode is replaced with transparent electrodes. We chose sputtered ITO herein due to its high optical transparency and electrical conductivity [29]. To avoid the sputtering damage, a 15-nm-thick SnO_2 deposited via atomic layer deposition (ALD) was applied as a protective layer. Meanwhile, the dense ALD deposited SnO_2 is beneficial to improving the stability of bifacial tandems as it can effectively protect the perovskite from humidity and oxygen [35]. Since rear illumination is incident from the bottom narrow-bandgap subcell (1.22 eV), the albedo illumination will mostly be absorbed by the bottom subcell, leading to current density increase only in bottom subcell while having little contribution to the top subcell. Therefore, to achieve current matching between two subcells under rear illumination, the current density of the top subcell should be elaborately optimized. Bandgap engineering is an effective way to tune the current matching. For this proposal, bifacial tandems with wide-bangap perovskite having various bandgaps (1.60, 1.62, 1.68, 1.73, 1.77 eV, determined from Tauc plot, shown in Additional file 1: Figure S1) were fabricated via adjusting the Br/(Br + I) ratio in $FA_{0.8}Cs_{0.2}Pb(I_{1-x}Br_x)$ perovskite [36].

To evaluate the performance gain under rear illumination, bifacial tandems were placed between two AM 1.5G solar simulators. The front illumination (wide-bandgap perovskite side) was set to an intensity of 100 mW cm^{-2}, while the rear illumination (narrow-bandgap perovskite side) was set with an adjustable intensity (0–100 mW cm^{-2}). Compared with monofacial tandems (1.77 eV-Mono) with 1.77 eV wide bandgap perovskte using opaque rear metal contact, the bifacial tandems (1.77 eV) exhibited a lower short current density (J_{sc})without rear illumination (Fig. 1d), since the rear transparent electrode in the bifacial tandems allow partial light pass through (Additional file 1: Figure S2). However, by harversting light from rear illumination (30 mW cm^{-2}) [32], the J_{sc} of bifacial tandems (1.77 eV) exhibits a comparable value to the monofacial tandems, and a slightly higher open circuit voltage as the rear illlumination increased the carriers density in the narrow-bandgap perovskite subcells.

To further explore the OPD gain from bifaciality, we tested the photovoltaic performance of bifacial tandems with wide-bandgap perovskites having different bangaps with and without a rear irradiance (30 mW cm^{-2}), as shown in Fig. 1c–f and Table 1. The typic *J-V* cuves and maxium power point (MPP) were presented in Additional file 1: Figure S3 and Table S1. This rear irradiance (30 mW cm^{-2}) is realistic in the real-world outdoor conditions [32]. In the absence of rear illumination, the OPD of all bifacial tandems with different bandgaps of wide-bandgap perovskite was lower than the monofacial tandems. Narrowing the bandgap of wide-bandgap perovskite, the J_{sc} of bifacial tandems steady decreased due to the higher current mismatch (Fig. 3b). Meanwhile, lowing the bandgap of wide-bandgap perovskite led to reduced open circuit voltage(V_{oc}) of bifacial tandems, which shows a similar trend of the single junction wide-bandgap solar cells(Additional file 1: Figure S4).

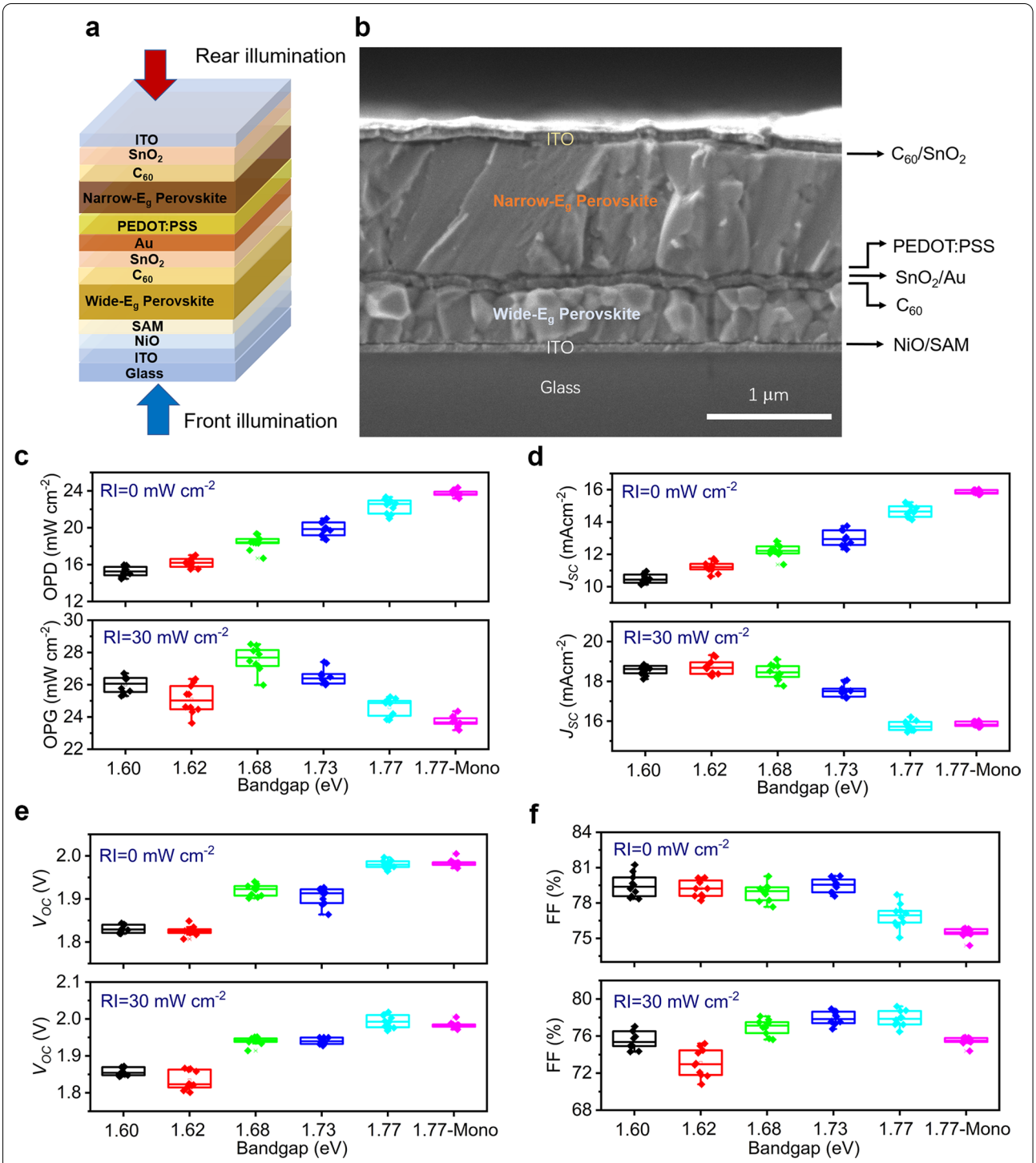

Fig. 1 **a** Schematic illustration and **b** cross-sectional scanning electron microscopy image of bifacial monolithic all-perovskite tandems. **c**-**f** Photovoltaic parameters for bifacial tandems with various bandgaps of wide-bandgap perovskite and monofacial tandems with bandgap of 1.77 eV (denoted as1.77-Mono), tested without and with 30 mW cm^{-2} rear irradiance (RI)

The fill factor (FF) increased as the decrease of bandgap of wide-bandgap perovskite, orignating from the higher current mismatch, as previous results for two-diode modelling [33]. However, with the assistance of 30 mW cm^{-2} rear illumination, all the bifacial tandems showed a higher OPD compared to the monofacial counterpart.

Table 1 Photovoltaic parameters for bifacial tandems with various bandgaps of wide-bandgap perovskite and monofacial tandem with bandgap of 1.77 eV, tested without and with 30 mW cm^{-2} rear irradiance (RI)

Bandgap (eV)	Rear irradiance (mW cm^{-2})	OPD mW cm^{-2}	J_{SC} (mA cm^{-2})	V_{OC} (V)	FF (%)
1.77-Mono	0	24.36 (23.72 ± 0.33)	16.02 (15.85 ± 0.12)	2.005 (1.984 ± 009)	75.82 (75.46 ± 0.43)
1.77	0	23.34 (22.35 ± 0.78)	15.13 (14.67 ± 0.38)	1.997 (1.980 ± 0.009)	77.29 (76.90 ± 1.02)
	30	25.25 (24.60 ± 0.55)	16.21 (15.76 ± 0.25)	1.991 (1.993 ± 0.017)	78.24 (78.29 ± 0.83)
1.73	0	21.00 (19.83 ± 0.77)	13.75 (12.99 ± 0.47)	1.924 (1.920 ± 0.014)	79.35 (79.51 ± 0.58)
	30	27.41 (26.50 ± 0.52)	18.00 (17.53 ± 0.31)	1.937 (1.940 ± 0.008)	78.65 (77.91 ± 0.71)
1.68	0	19.29 (18.40 ± 0.79)	12.61 (12.23 ± 0.39)	1.926 (1.906 ± 0.021)	79.39 (78.90 ± 0.74)
	30	28.51 (27.60 ± 0.78)	18.83 (18.48 ± 0.40)	1.938 (1.941 ± 0.011)	78.13 (76.96 ± 0.84)
1.62	0	17.03 (16.20 ± 0.51)	11.58 (11.20 ± 0.33)	1.835 (1.826 ± 0.011)	80.15 (79.25 ± 0.71)
	30	26.36 (25.09 ± 0.90)	19.24 (18.71 ± 0.38)	1.822 (1.834 ± 0.026)	75.19 (73.11 ± 1.52)
1.60	0	15.91 (15.26 ± 0.53)	10.95 (10.49 ± 0.29)	1.840 (1.830 ± 0.009)	78.95 (79.48 ± 0.98)
	30	26.71 (26.02 ± 0.55)	18.85 (18.55 ± 0.24)	1.852 (1.857 ± 0.011)	76.52 (75.53 ± 0.97)

Impresively, at the present of rear illumination, the bifacial tandems with 1.68 eV wide-bandgap perovksite show a best OPD of 28.51 mW cm^{-2} and a average OPD of 27.60 mW cm^{-2}, which was much higher than the OPD of monofacial tandems with a best value of 24.36 mW cm^{-2} and a average value of 23.72 mW cm^{-2}. Meanwile, our bifacial all-perovskite also show a high OPD compared with other reported bifaical solar cells, such as bifacial single-junction and bifacial perovskite/Si tandem solar cells (Additional file 1: Table S1). The OPD gain of the bifacial tandems with rear illumination mainly thanks to the noticeable boost of J_{sc} as the the decrease of the bandgap of wide-bandgap perovksite. Simutaneously, the increament of open circuit voltage of bifacial tandems with rear illumination benefiting from the rear illumination also contributed to the OPD gain.

To understand the effect of albedo on the photovoltaic performance of bifacial all-perovskite tandems, we investigated the evolution of photovoltaic parameters for bifacial tandems with different bandgaps of wide-bandgap perovskite under various rear illumination, ranging from 0 to 100 mW cm^{-2}, shown in Fig. 2a–d. With the increase of rear irradiance, the J_{sc} of the bifacial tandems firstly raised rapidly, then kept steady for higher rear irradiance. As expected, the lower the bandgap of wide-bandgap perovskite, the higher saturated J_{sc} and higher rear illumination required to reach the staturated J_{sc} of bifacial tandems. As the bandgap of wide-bandgap perovskite decrease, the wider spectrum of photons are absorbed by top subcells raise, reducing the current density of bottom subcells (Fig. 3b). Therefore, higher rear illumination was needed to achieve current matching of the two subcells for bifacial tandems. The V_{oc} of the bifacial tandems also showed an increase trend with the rear illumination, which increased the photogenerated charge carries in the bottom subcells. For all bifacial tandems, the FF showed a V-shaped recovery, and the minimal FF located around the minimal rear irradiance needed for the saturated J_{sc}.This phenomenon was expected to stem from the current matching condition in the bifacial tandems [33]. The minimal FF appeares near the current matching condition, while both the bottom cell curent limitation and top cell curent limition condition can get a higher FF. The OPD showed a similar trend of J_{sc} with the increase in rear irradiance. It's worth noting that once the rear irradiance exceed 25 mW cm^{-2}, the OPD of all bifacial tandems with different bandgaps overtakes the monofacial counterpart. With a rear irradiance of 50 mW cm^{-2}, around 29.3 mW cm^{-2} of OPD can be achieved for bifacial tandem with 1.68 and 1.60 eV wide-bandgap perovskite. The 50 mW cm^{-2} rear irradiance is achievable for highly reflective surface, such as fiberglass rooftop [27].

With those result, we can estimated the pratical OPD potential of the bifaical monolithic all-perovskite

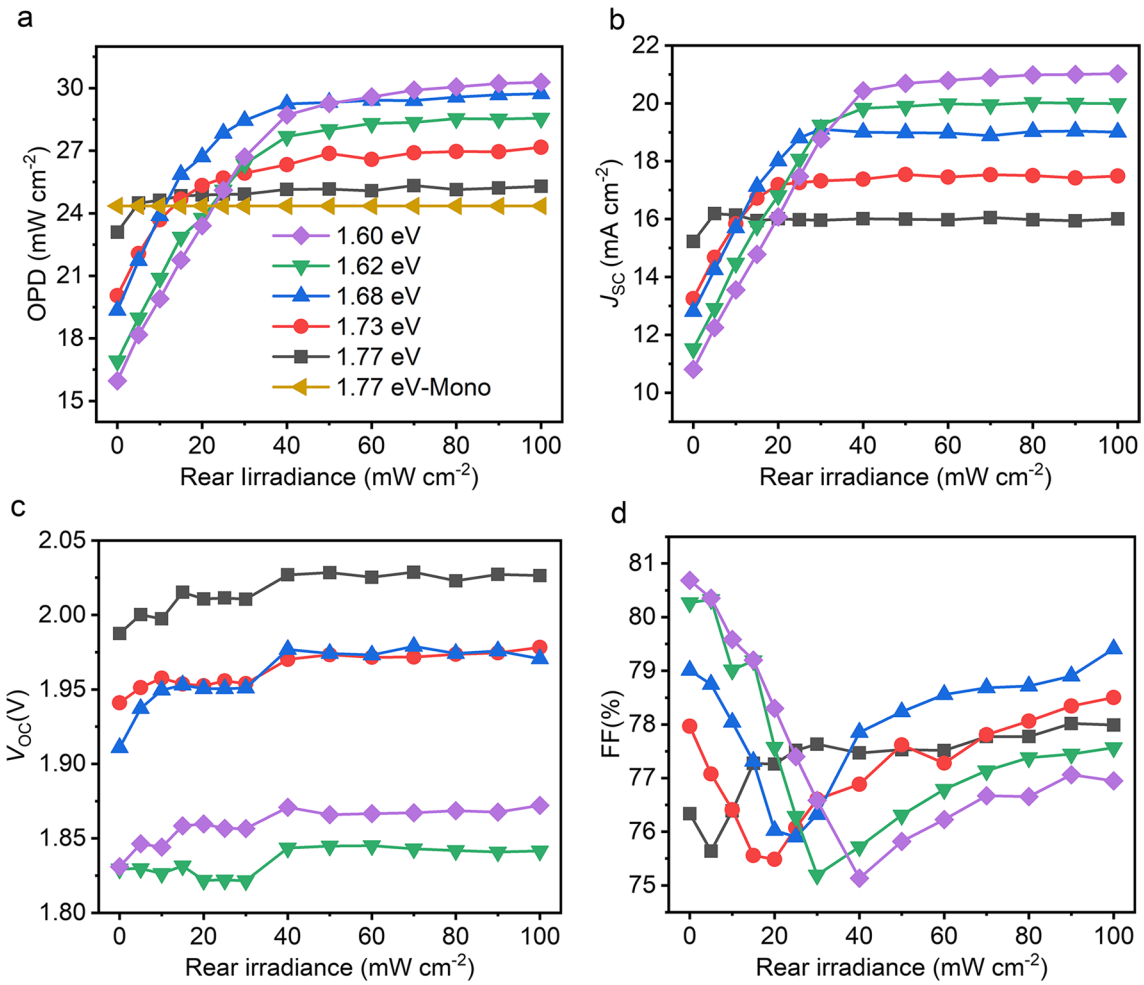

Fig. 2 Photovoltaic parameters of bifacial tandems with wide-bandgap perovskites having different bandgaps under various rear irradiance. Performance of monofacial tandem is included for comparison

tandems. With a 30 mW cm^{-2} realistic rear irradiance, our bifacial already showed a relative 17% OPD improvement compared to the monofacial tandems, from 24.31 mW cm^{-2} of monofacail tandems to 28.51 mW cm^{-2} of bifacial tandems (1.68 eV). An over 20% OPD gain would be practical by further optimimied the current matching by using antireflctive layer and light trapping strategies. When taking the reported empirical limits of 33.6 mW cm^{-2} for the monofacial all-perovskite tandems [37], a 20% OPD gain of the bifaical configuration will result in a OPD of 40.32 mW cm^{-2} with a 30 mW cm^{-2} realistic rear irradiance.

As discussed before, the OPD gain of tandems with bifacial configuration primarily benefits from the boost of J_{sc} as a result of the synergy of bandgap engineering and bifaciality. Hence, having an insight into the current matching conditions of the bifacial tandems is highly desired. Figure 3a shows the EQE spectrum of bifacial tandems for front illumination with different bandgaps of wide-bandgap perovskite. As expected, decreasing the bandgaps widened the EQE response spectrum of wide-bandgap subcells, reducing the EQE response of the narrow-bandgap subcells in the overlap region. As a result, the current mismatch enlarged with the decrease of bandgap of wide-bandgap perovskite. Therefore, under the operation condition without rear irradiance, the J_{sc} of the bifacial tandems dropped when lowing the bandgap of wide-bandgap perovskite (Fig. 3b). With the presence of rear irradiance (100 mW cm^{-2}), the trend of J_{sc} as the function of bandgap for bifacial tandems was reversed (Fig. 3b). Furthermore, Fig. 3c shows the EQE spectrum of bifacial tandems for rear illumination with different bandgaps of wide-bandgap perovskite. For all bandgaps, the low-bandgap

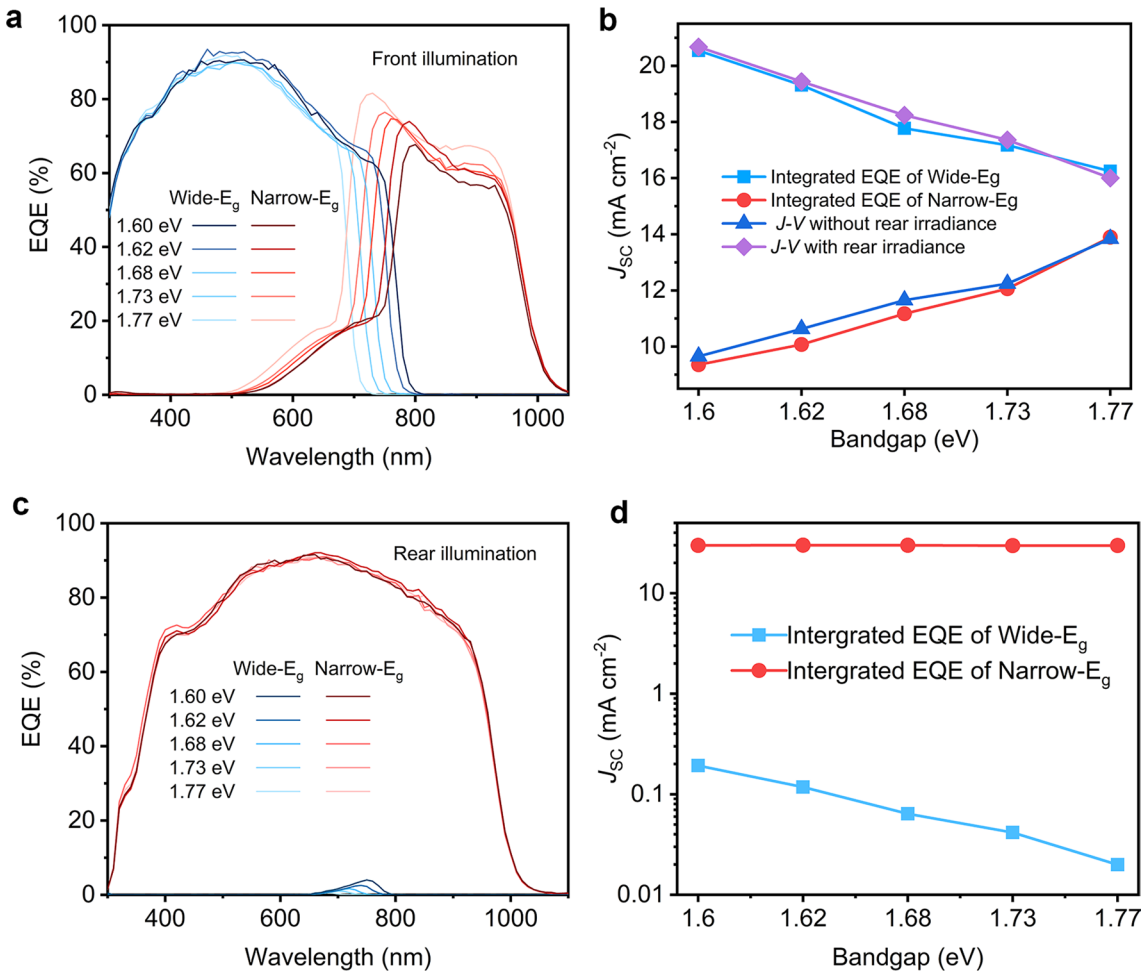

Fig. 3 **a** External quantum efficiency (EQE) curves of wide-bandgap (Wide-E_g) and narrow-bandgap (Narrow-E_g) subcells in bifacial all-perovskite tandems with various top-cell bandgaps under front (glass) side illumination. **b** J_{sc} of bifacial all-perovskite tandems with various bandgaps obtained from integrated EQE and *J-V* curves under front(glass) side illumination. For J_{sc} from *J-V* curves, the measurements were carried out with and without rear irradiance. **c** EQE spectrum of bifacial all-perovskite tandems with various bandgaps under rear (film) side illumination. **d** J_{sc} of bifacial all-perovskite tandems with various bandgaps obtained from integrated EQE under rear (film) side illumination

subcells showed almost the same EQE response with an integrated J_{sc} around 30 mA cm^{-2}, which agree well with the optical absorptance spectra (Additional file 1: Figure S6). The EQE response of all wide-bandgap subcells was very low compared to low-bandgap subcells for the rear illumination. Those results further verified the necessity for the bandgap engineering to increase the current in the top subcells, and hence to achieve current matching in the bifacial configuration, as the rear illumination mainly contributed to the bottom subcells. In addition, we note that using thicker wide bandgap perovskite can also be used for higher current in the top subcells, which can be explored in the future.

In order to reveal the output power potential of bifacial tandems under real-world solar illumination, we carry out the energy yield simulation. Six natural and artificial grounds were used to cover a wide range of mean albedo (300–1100 nm) from 13 to 95%. The reflection spectrum of the grounds and the corresponding mean albedo (R_A) were presented in Additional file 1: Figure S7. Moreover, two locations with two typical climates were used for the simulation, New York with a temperate climate and Arizona with an arid climate. As shown in Fig. 4, the optimum bandgap of WBG perovskite for bifacial tandems shifts to a lower value with the increase of albedo, showing the same trend as our experimental result (Fig. 2). In both two locations and under six grounds, energy yield was improved with albedo for both monofacial and bifacial tandems. The energy yield gain of bifacial tandems was

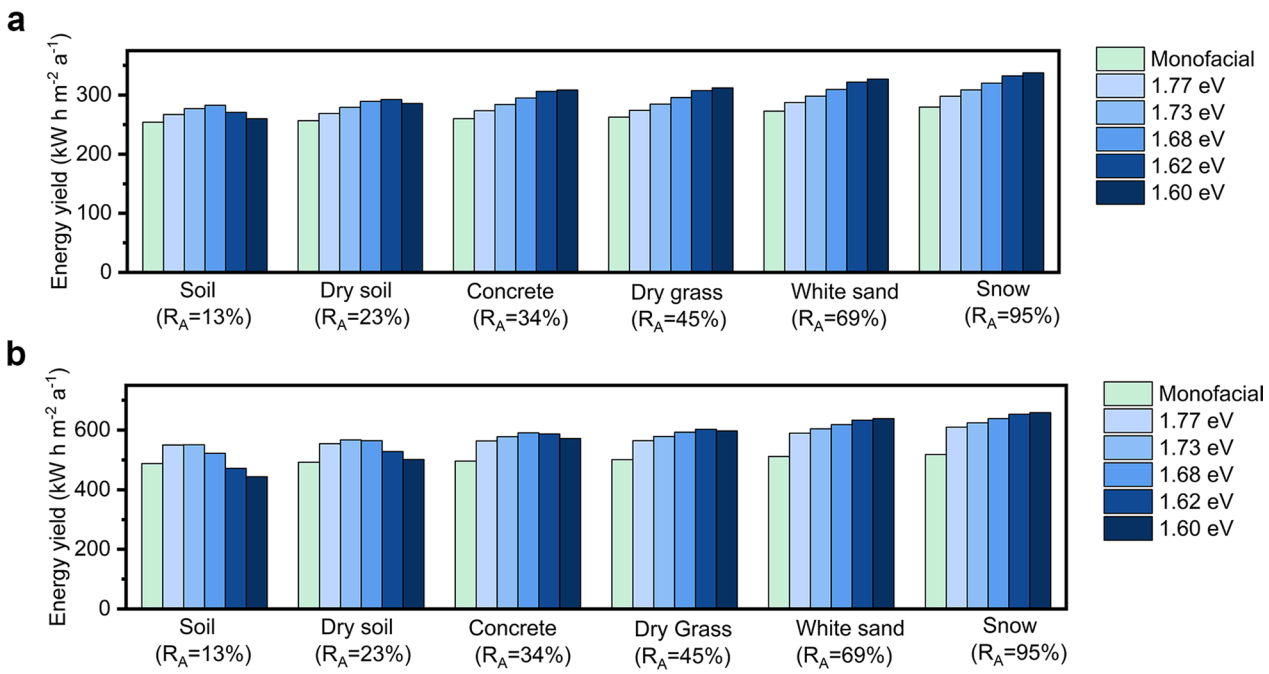

Fig. 4 Energy yield calculation of monofacial and bifacial tandems with various bandgaps under six grounds (soil, dry soil, concrete, dry grass, white sand, snow) with a wide range mean albedo (R_A), for two locations with different climate: **a** New York features a temperate climate and **b** Arizona an arid climate

more notable as the rear side harvested more reflected light from the ground than the front light. It is worth noting that benefits from the albedo, the energy yield of bifacial tandems outperforms the monofacial counterpart even with a very low albedo of 13% for soil. Under a moderate albedo of 34% for concrete ground, the best bifacial tandems in New York and Arizona show an 18% and 15% energy yield gain compared to the monofacial tandems. The energy yield gain of the best tandems in New York and Arizona can be further improved to 21% and 26% under snow ground with a high albedo of 95%. To further increase the energy yield for the bifacial tandems, thickness optimization of stack layers and solar tracking technique should be further explored.

3 Discussion and conclusion

The bifacial all-perovskite monolithic tandems were demonstrated by using transparent rear electrodes, which enable the harvest of light impacting the rear side of the tandems. Coupling with the current gain in the bottom subcells by the assistance of the albedo, and the current increase in top subcells via bandgap engineering, the bifacial tandems showed remarkable performance improvement than the monofacial tandems. With a realistic rear illumination of 30 mW cm^{-2}, the OPD with a value of 28.51 mW cm^{-2} can be achieved by bifacial tandems, outperforming the monofacial tandems with a value of 24.3 mW cm^{-2}. In this work, only the bandgap of top subcell was adjusted to achieved current matching of bifacial tandems with rear illumination, which was valid for albedo below 40% (Fig. 2). While for albedo over 40%, the current density of the tandems saturated (Fig. 2). To tackle this issue, we propose further decreasing the bandgap of the top subcells or increasing the bandgap of bottom subcells. Moreover, the bifacial tandems have the potential for higher stability over the monofacial architecture, since the use of ALD-deposited SnO_2 and sputtered transparent conduction oxide (ITO) as rear contacts can avoid the halide corrosion of rear electrodes, and the reduction of bromide content in the top cell can relieve the halide segregation issue [24]. By performing energy yield calculation, bifacial tandems showed substantial energy yield gain in the real-world conditions with various presentive grounds in different climatic conditions. As the bifacial all-perovskite tandems aim to harvest light at rear side to boost OPD, they are expected to be applicated at the utility scale. We also note that our bifacial all-perovskite tandem fabricated on grid glass substrate can be also processed on flexible substrate for flexible bifacial all-perovskite tandem, which will be challenging for bifacial perovskite/silicon tandem. Meanwhile, the climate conditions and the grounds directly impact the intensity and spectrm of the albedo, therefore the custmized bifacial tandems with different bandgap of

top subcells are required for various climate condition and grounds. To well ulitize the albedo over the daytime, solar tracking technique will be an attractive technology for bifacial tandems. This work reveals the potential of bifaical all-perovskite tandems as a new device architecutre for higher output power with enhanced stability.

4 Materials and methods

4.1 Materials

All materials were used as received without further purification. The organic halide salts (FAI and MAI with purity of > 99%) were purchased from Greatcell Solar Materials. PbI2 (99.99%, trace metals basis) and $PbBr_2$ (99.99%, trace metals basis), 2PACz (> 98.0%) and MeO-2PACz (> 98.0%) were purchased from TCI. SnF2 (99%), CsI (99.999%), tin powders (< 150 μm, 99.5%), dimethylformamide (DMF, 99.8% anhydrous), dimethyl sulfoxide (DMSO, 99.9% anhydrous), chlorobenzene (99.8% anhydrous) and ethylacetate (99.8% anhydrous) were purchased from Sigma-Aldrich. The C60 was purchased from Nano-C. PEDOT-PSS aqueous solution (Al 4083) was purchased from Heraeus Clevios. ITO target (In_2O_3:SnO_2 = 90:10 wt%, 99.99%) was purchased from ZhongNuo Advanced Material Technology Co., Ltd. Tetrakis(dimethylamino) tin(iv) (99.9999%) was purchased from Nanjing Ai Mou Yuan Scientific Equipment.

4.2 Device fabrication

The patterned ITO glass substates (25 × 25 mm, 20 Ω sq^{-1}) were firstly cleaned via sonication in water, acetone, and isopropanol for 15 min. Then, the cleaned ITO glass substrates were treated under UV-ozone for 15 min. 15 mg ml^{-1} of NiO in water was spin-coated on ITO at 4000 rpm for 30 s and annealed at 100 ℃ for 5 min. Following, a 1 mmol/L mixture self-assembled monolayers (2PACZ:MeO-2PACZ = 3:1,molar ratio) in isopropanol was spin-coated on NiO film at 4000 rpm for 20 s. After annealing at 100 ℃ for 10 min, the substates were washed twice by isopropanol with a 4000 rpm, 13 s spin-coating program, and then annealed at 100 ℃ for 5 min.

To make wide-bandgap perovskite (450 nm) with different bandgap, the ratio of $PbBr_2/(PbI_2 + PbBr_2)$ of $FA_{0.8}Cs_{0.2}Pb(I_{1-x}Br_x)_3$ perovkite precuror (1.2 M) varied from 0.13:1 to 0.40:1, while the the molar ratio of FAI/CsI and $(FAI + CsI)/(PbI_2 + PbBr_2)$ were 0.8:0.2 and 1;1, respectively. The perovskite precuror dissolved in DMF/DMSO (4:1, volume ratio) was spin-coated at 2000 rpm for 5 s, and then 4000 rpm for 35 s in the glovebox. Chlorobenzene (100 ml) as antisolvent was dropped onto the perovskite 25 s after the second spin-coating program of wide-bandgap perovskite film deposition. Subsequently, the perovskite was annealed at 100℃ for 15 min. After cooling, a 26 nm C_{60} by thermal evaporation and 20 nm SnO_2 by atomic layer deposition (ALD) using precursors of tetrakis (dimethylamino) tin (iv) at a substate temperature of 85 ℃ were grown. A around 1 nm Au cluster was then thermally evaporated on SnO_2. PEDOT:PSS was deposited on the top of Au cluster by spin-coating at 4000 rpm and annealed at 150 ℃ for 10 min in the air. The $FA_{0.7}MA_{0.3}Pb_{0.5}Sn_{0.5}I_3$ perovskite precursor (2.2 M) was prepared by dissolving $MAI/FAI/PbI_2/SnI_2/SnF_2$ with a ratio of 0.3:0.7:0.5:0.5:0.1 in DMF/DMSO (2:1, volume ratio) mixture solvent. Tin powders (5 mg ml^{-1}) were added into the precursor solution as antioxidant. The narrow-bandgap perovskite films (1000 nm) were deposited on the PEDOT:PSS film in the glovebox by a two-step spin-coating program: the perovskite precursor solution was firstly spin-coated at 1000 rpm for 10 s, then at 5000 rpm for 50 s. Ethyl acetate (200 ml) as antisolvent was dropped onto the narrow-bandgap perovskite 20 s after the second spin-coating program of perovskite film deposition. Next, a 26 nm C_{60} was deposited by thermal evaporation and a 20 nm SnO_2 deposited by ALD at 85℃. ITO (80 nm) was sputtered on top of SnO_2 through a mask. Finally, a 150 nm Ag frame was thermally evaporated on top of ITO.

4.3 Device and film characterization

The curent density–voltage (*J-V*) measurement of bifacial tandems with rear illumination was carried out using a Kithley 4200 source meter. A Xenon lamp solar simulator with AM 1.5G spectrum (100 mW cm^{-2}) was used as front illumination. For the rear illumination, the second Xenon lamp solar simulator with AM 1.5G spectrum (0–100 mW cm^{-2}) used to simulate the real albedo. The power density of the rear illumination was calibared by using a standard Si solar cell form Word PV scale. The area of the tandems was 0.09 cm^2 (0.3 cm × 0.3 cm) defined by two metal masks coved on both sides of the devices. For the EQE measuremnt, bias illumination generated by light-emitting diodes (LEDs) with emission peaks at 850 and 460 nm was used to measure the top and bottom subcells. The cross-section scanning electron microscopy (SEM) image was carried out using a TESCAN microscope. Optical absorption of the perovskite films was measured using a Lambda 950 ultraviolet–visible spectrophotometer.

4.4 Energy yield simulation

The energy yield simulation was proformed using an open-assess software EYcalc developed by Schmager et.al [38]. The angular and wavelength-resolved irradiance data was generated by the model of atmospheric radiative transfer of sunshine (SMARTS) using typical meteorological year (TMY3) spectral data from NREL [39, 40]. The albedo spectrums of the grounds used for

the simulation are from the ecosystem spacebornethermal radiometer experiment on space station (ECOSTRESS) spectrallibrary [41]. For the optical simulation, the optical constant was utilized from our previous work [42]. Especially, optical constant of WBG perovskites with difference bandgaps were derivered by translating the data of 1.78 eV WBG perovskite along the wavelength axis [43]. One-diode equivalent circuit model was used to extracted the electric parameter (idality factor, series resistance, shunt resistance, reverse saturation current) of the WBG and NBG subcells (Additional file 1: Figure S8 and Table S4) [44]. We keep the electric parameters the same for WBG perovskite with different bandgaps except for the reverse saturation current, which follows the optoelctronic reciprocity theorem [45]. For the energy yield, the cells were fixed toward the south with a tilt angle of 40º and 35 º in New York and Arizona.

Supplementary Information

The online version contains supplementary material available at https://doi.org/10.1186/s43593-022-00028-w.

Additional file 1: Figure S1. (a) Tauc plot of $FA_{0.8}Cs_{0.2}Pb(I_{1-x}Br_x)_3$ perovskite and (b) a linear relationship of the bandgap (E_g) as a function of Br composition (x). **Figure S2.** EQE spectra of monofacial (Mono-1.77 eV) and bifacial tandem (1.77 eV). **Figure S3.** (a,b) *J-V* curves and (c,d) maximum power point (MPP) tracking for bifacial tandems with various bandgaps of wide-bandgap perovskite and monofacial tandems (1.77-Mono), tested without and with 30 mW cm^{-2} rear irradiance (RI). **Table S1.** Photovoltaic parameters extracted from Figure S2 for typic bifacial and monofacil tandems. **Table S2 .**Output power density of various monofacial and bifacial solar cells. **Figure S4.** (a) *J-V* curves and (b) EQE spectrum of wide-bandgap single-junction solar cells with different bandgap. **Table S3.** Photovoltaic parameters of of wide-bandgap single-junction solar cells with different bandgap. **Figure S5.** (a) *J-V* curves and (b) EQE spectrum of low-bandgap single junction solar cells. **Figure S6.** Optical tansmittance, reflectance and absorptance of bifacial and monofacial tandems under front (a) and (b) rear illumination. **Figure S7.** Reflection spectra and mean albedo (300-1100 nm) of six grounds. **Figure S8.** Experimental and simulated *J-V* curves of WBG (1.77 eV) and NBG perovskite solar cells. **Table S4.** Diode parameters used to simulte *J-V* curves of WBG (1.77 eV) and NBG perovskite solar cells.

Acknowledgements
Not applicable.

Author contributions
HL led the device fabrication, simulation and characterazation. RW, HG, and RL contributed on device fabrication. MZ, PW, KX contributed on characterazation. HL, HT preparated the manuscript, and all authours read and improved the manuscript. HT conceived the idea and headed the preject.

Funding
This work was financially supported by the National Key R&D Program of China (2018YFB1500102), National Natural Science Foundation of China (61974063, U21A2076), Natural Science Foundation of Jiangsu Province (BK20202008, BK20190315), Fundamental Research Funds for the Central Universities (0213/14380206; 0205/14380252), Frontiers Science Center for Critical Earth Material Cycling Fund (DLTD2109), and Program for Innovative Talents and Entrepreneur in Jiangsu.

Data availability
The datasets used and/or analysed during the current study are available from the corresponding author on reasonable request.

Declarations

Competing interests
The authors declare no conflict of interest.

Received: 28 July 2022 Revised: 4 September 2022 Accepted: 7 September 2022
Published online: 17 October 2022

References

1. A. Kojima, K. Teshima, Y. Shirai, T. Miyasaka, Organometal halide perovskites as visible-light sensitizers for photovoltaic cells. J. Am. Chem. Soc. **131**, 6050–6051 (2009)
2. H. Min et al., Perovskite solar cells with atomically coherent interlayers on SnO2 electrodes. Nature **598**, 444–450 (2021)
3. W. Shockley, H.J. Queisser, Detailed balance limit of efficiency of p-n junction solar cells. J. Appl. Phys. **32**, 510–519 (1961)
4. A.D. Vos, Detailed balance limit of the efficiency of tandem solar cells. J. Phys. D. Appl. Phys. **13**, 839–846 (1980)
5. F. Hao, C.C. Stoumpos, R.P.H. Chang, M.G. Kanatzidis, Anomalous band gap behavior in mixed Sn and Pb perovskites enables broadening of absorption spectrum in solar cells. J. Am. Chem. Soc. **136**, 8094–8099 (2014)
6. R.E. Beal et al., Cesium lead halide perovskites with improved stability for tandem solar cells. J. Phys. Chem. Lett. **7**, 746–751 (2016)
7. S.D. Stranks et al., Electron-hole diffusion lengths exceeding 1 micrometer in an organometal trihalide perovskite absorber. Science **342**, 341–344 (2013)
8. S. De Wolf et al., Organometallic halide perovskites: sharp optical absorption edge and its relation to photovoltaic performance. J. Phys. Chem. Lett. **5**, 1035–1039 (2014)
9. Z. Ni et al., Resolving spatial and energetic distributions of trap states in metal halide perovskite solar cells. Science **367**, 1352–1358 (2020)
10. J.P. Mailoa et al., A 2-terminal perovskite/silicon multijunction solar cell enabled by a silicon tunnel junction. Appl. Phys. Lett. **106**, 121105 (2015)
11. K. Daehan et al., Efficient, stable silicon tandem cells enabled by anion-engineered wide-bandgap perovskites. Science **368**, 155–160 (2020)
12. A.-A. Amran et al., Monolithic perovskite/silicon tandem solar cell with >29% efficiency by enhanced hole extraction. Science **370**, 1300–1309 (2020)
13. Q. Han et al., High-performance perovskite/Cu (In, Ga) Se2 monolithic tandem solar cells. Science **361**, 904–908 (2018)
14. A. Al-Ashouri et al., Conformal monolayer contacts with lossless interfaces for perovskite single junction and monolithic tandem solar cells. Energy Environ. Sci. **12**, 3356–3369 (2019)
15. W. Chen et al., Monolithic perovskite/organic tandem solar cells with 23.6% efficiency enabled by reduced voltage losses and optimized interconnecting layer. Nat. Energ **7**, 229–237 (2022)
16. K.O. Brinkmann et al., Perovskite–organic tandem solar cells with indium oxide interconnect. Nature **604**, 280–286 (2022)
17. R. Lin et al., All-perovskite tandem solar cells with improved grain surface passivation. Nature **603**, 73–78 (2022)
18. G.E. Eperon et al., Perovskite-perovskite tandem photovoltaics with optimized band gaps. Science **354**, 861–865 (2016)
19. I. Celik et al., Energy payback time (EPBT) and energy return on energy invested (EROI) of perovskite tandem photovoltaic solar cells. IEEE J. Photovoltaics **8**, 305–309 (2018)
20. Z. Li et al., Cost analysis of perovskite tandem photovoltaics. Joule **2**, 1559–1572 (2018)
21. A.F. Palmstrom et al., Enabling flexible all-perovskite tandem solar cells. Joule **3**, 2193–2204 (2019)
22. S. Moghadamzadeh et al., In2O3: H-based hole-transport-layer-free tin/lead perovskite solar cells for efficient four-terminal all-perovskite tandem solar cells. ACS Appl. Mater. Interfaces **13**, 46488–46498 (2021)

23. C. Li, Y. Wang, W.C.H. Choy, Efficient interconnection in perovskite tandem solar cells. Small Methods **4**, 2000093 (2020)
24. M.A. Green et al., Solar cell efficiency tables (version 60). Prog. Photovoltaics Res. Appl. **30**, 687–701 (2022)
25. National Renewable Energy Laboratory, Best Research-Cell Efficiency Chart. https://www.nrel.gov/pv/cell-efficiency.html.
26. F. Fu et al., Low-temperature-processed efficient semi-transparent planar perovskite solar cells for bifacial and tandem applications. Nat. Commun. **6**, 8932 (2015)
27. Z. Song et al., Assessing the true power of bifacial perovskite solar cells under concurrent bifacial illumination. Sustain. Energ. Fuels **5**, 2865–2870 (2021)
28. S.-H. Lim et al., Semi-transparent perovskite solar cells with bidirectional transparent electrodes. Nano Energy **82**, 105703 (2021)
29. K.A. Bush et al., Thermal and environmental stability of semi-transparent perovskite solar cells for tandems enabled by a solution-processed nanoparticle buffer layer and sputtered ITO electrode. Adv. Mater. **28**, 3937–3943 (2016)
30. M.A. Alam, M.R. Khan, Thermodynamic efficiency limits of classical and bifacial multi-junction tandem solar cells: an analytical approach. Appl. Phys. Lett. **109**, 173504 (2016)
31. A. Onno et al., Predicted power output of silicon-based bifacial tandem photovoltaic systems. Joule **4**, 580–596 (2020)
32. J. Lehr et al., Energy yield of bifacial textured perovskite/silicon tandem photovoltaic modules. Sol. Energy Mater. Sol. Cells **208**, 110367 (2020)
33. M. De Bastiani et al., Efficient bifacial monolithic perovskite/silicon tandem solar cells via bandgap engineering. Nat. Energy **6**, 167–175 (2021)
34. M. Ryyan Khan, M.A. Alam, Thermodynamic limit of bifacial double-junction tandem solar cells. Appl. Phys. Lett. **107**, 223502 (2015)
35. H. Gao et al., Thermally stable all-perovskite tandem solar cells fully using metal oxide charge transport layers and tunnel junction. Sol. RRL. **5**, 2100814 (2021). https://doi.org/10.1002/solr.202100814
36. K.A. Bush et al., Compositional engineering for efficient wide band gap perovskites with improved stability to photoinduced phase segregation. ACS. Energ. Lett. **3**, 428–435 (2018)
37. M. Jošt, L. Kegelmann, L. Korte, S. Albrecht, Monolithic perovskite tandem solar cells: a review of the present status and advanced characterization methods toward 30% efficiency. Adv. Energ. Mater. **10**, 1904102 (2020)
38. R. Schmager et al., Methodology of energy yield modelling of perovskite-based multi-junction photovoltaics. Opt. Express. **27**, A507–A523 (2019)
39. S. Wilcox, W. M. (2008) Users manual for TMY3 data sets. *NREL* 51.
40. C.A. Gueymard, Parameterized transmittance model for direct beam and circumsolar spectral irradiance. Sol. Energ. **71**, 325–346 (2001)
41. A.M. Baldridge, S.J. Hook, C.I. Grove, G. Rivera, The ASTER spectral library version 2.0. Remote Sens. Environ. **113**, 711–715 (2009)
42. K. Xiao et al., All-perovskite tandem solar cells with 24.2% certified efficiency and area over 1 cm^2 using surface-anchoring zwitterionic antioxidant. Nat. Energ. **5**, 870–880 (2020)
43. S. Manzoor et al., Optical modeling of wide-bandgap perovskite and perovskite/silicon tandem solar cells using complex refractive indices for arbitrary-bandgap perovskite absorbers. Opt. Express **26**, 27441–27460 (2018)
44. M.T. Hörantner, H.J. Snaith, Predicting and optimising the energy yield of perovskite-on-silicon tandem solar cells under real world conditions. Energ. Environ. Sci. **10**, 1983–1993 (2017)
45. U. Rau, Reciprocity relation between photovoltaic quantum efficiency and electroluminescent emission of solar cells. Phys. Rev. B **76**, 85303 (2007)